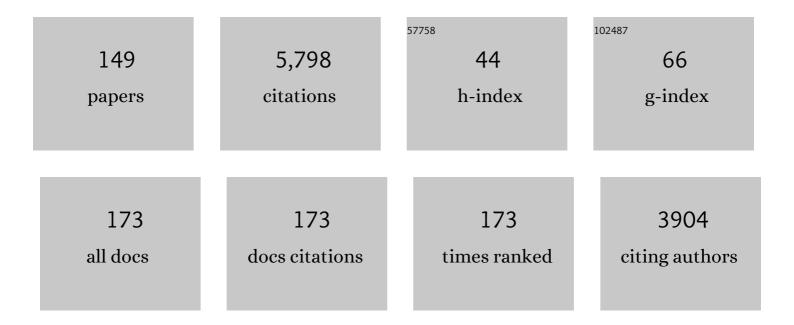
Steven M. Reddy

List of Publications by Year in descending order

Source: https://exaly.com/author-pdf/4658327/publications.pdf Version: 2024-02-01



#	Article	IF	CITATIONS
1	Timing of crystallization of the lunar magma ocean constrained by the oldest zircon. Nature Geoscience, 2009, 2, 133-136.	12.9	189
2	The geometry and timing of orogenic extension: an example from the Western Italian Alps. Journal of Metamorphic Geology, 1999, 17, 573-589.	3.4	129
3	A pressure-temperature phase diagram for zircon at extreme conditions. Earth-Science Reviews, 2017, 165, 185-202.	9.1	128
4	Quantitative characterization of plastic deformation of zircon and geological implications. Contributions To Mineralogy and Petrology, 2007, 153, 625-645.	3.1	127
5	Crystal-plastic deformation of zircon: A defect in the assumption of chemical robustness. Geology, 2006, 34, 257.	4.4	122
6	Temporal constraints on Palaeoproterozoic eclogite formation and exhumation (Usagaran Orogen,) Tj ETQq0 0 C) rgBT /Ove	erlock 10 Tf 5

7	Naturally occurring gold nanoparticles and nanoplates. Geology, 2008, 36, 571.	4.4	110
8	In situ multiple sulfur isotope analysis by SIMS of pyrite, chalcopyrite, pyrrhotite, and pentlandite to refine magmatic ore genetic models. Chemical Geology, 2016, 444, 1-15.	3.3	108
9	The carbonate tectonic units of northern Calabria (Italy): a record of Apulian palaeomargin evolution and Miocene convergence, continental crust subduction, and exhumation of HP–LT rocks. Journal of the Geological Society, 2007, 164, 1165-1186.	2.1	107
10	A 40Ar/39Ar laser probe study of micas from the Sesia Zone, Italian Alps: implications for metamorphic and deformation histories. Journal of Metamorphic Geology, 1996, 14, 493-508.	3.4	103
11	Metallogeny and its link to orogenic style during the Nuna supercontinent cycle. Geological Society Special Publication, 2016, 424, 83-94.	1.3	101
12	Trench-parallel fast axes of seismic anisotropy due to fluid-filled cracks in subducting slabs. Earth and Planetary Science Letters, 2009, 283, 75-86.	4.4	99
13	Kinematic reworking and exhumation within the convergent Alpine Orogen. Tectonophysics, 2003, 365, 77-102.	2.2	96
14	Nanoscale gold clusters in arsenopyrite controlled by growth rate not concentration: Evidence from atom probe microscopy. American Mineralogist, 2016, 101, 1916-1919.	1.9	94
15	Evolution of the Singhbhum Craton and supracrustal provinces from age, isotopic and chemical constraints. Earth-Science Reviews, 2019, 193, 237-259.	9.1	89
16	Palaeoproterozoic supercontinents and global evolution: correlations from core to atmosphere. Geological Society Special Publication, 2009, 323, 1-26.	1.3	87
17	Resolution of impactâ€related microstructures in lunar zircon: A shockâ€deformation mechanism map. Meteoritics and Planetary Science, 2012, 47, 120-141.	1.6	87
18	Nanogeochronology of discordant zircon measured by atom probe microscopy of Pb-enriched dislocation loops. Science Advances, 2016, 2, e1601318.	10.3	86

dislocation loops. Science Advances, 2016, 2, e1601318.

#	Article	IF	CITATIONS
19	Ion-probe dating of 1.2Ga collision and crustal architecture in the Namaqua-Natal Province of southern Africa. Precambrian Research, 2007, 158, 79-92.	2.7	85
20	Atom Probe Tomography: Development and Application to the Geosciences. Geostandards and Geoanalytical Research, 2020, 44, 5-50.	3.1	84
21	A terrestrial perspective on using <i>ex situ</i> shocked zircons to date lunar impacts. Geology, 2015, 43, 999-1002.	4.4	80
22	Relationship among titanium, rare earth elements, U–Pb ages and deformation microstructures in zircon: Implications for Ti-in-zircon thermometry. Chemical Geology, 2011, 280, 33-46.	3.3	79
23	Laser-probe 40Ar/39Ar investigation of a pseudotachylyte and its host rock from the Outer Isles thrust, Scotland. Geology, 1994, 22, 443.	4.4	73
24	Enhanced diffusion of Uranium and Thorium linked to crystal plasticity in zircon. Geochemical Transactions, 2006, 7, 10.	0.7	72
25	Zircon U–Pb strain chronometry reveals deep impact-triggered flow. Earth and Planetary Science Letters, 2009, 277, 73-79.	4.4	72
26	Gold nuggets: supergene or hypogene?. Australian Journal of Earth Sciences, 2007, 54, 959-964.	1.0	71
27	Gold, arsenic, and copper zoning in pyrite: A record of fluid chemistry and growth kinetics. Geology, 2019, 47, 641-644.	4.4	71
28	Mechanisms of deformation-induced trace element migration in zircon resolved by atom probe and correlative microscopy. Geochimica Et Cosmochimica Acta, 2016, 195, 158-170.	3.9	64
29	Microstructural constraints on the mechanisms of the transformation to reidite in naturally shocked zircon. Contributions To Mineralogy and Petrology, 2017, 172, 1.	3.1	64
30	Morphology and microstructure of chromite crystals in chromitites from the Merensky Reef (Bushveld Complex, South Africa). Contributions To Mineralogy and Petrology, 2013, 165, 1031-1050.	3.1	61
31	Complex high-strain deformation in the Usagaran Orogen, Tanzania: structural setting of Palaeoproterozoic eclogites. Tectonophysics, 2003, 375, 101-123.	2.2	58
32	Effects of geodynamic setting on the redox state of fluids released by subducted mantleÂlithosphere. Lithos, 2017, 278-281, 26-42.	1.4	57
33	Kinematic linkage between internal zone extension and shortening in more external units in the NW Alps. Journal of the Geological Society, 2001, 158, 439-443.	2.1	49
34	Deformation-related microstructures in magmatic zircon and implications for diffusion. Contributions To Mineralogy and Petrology, 2009, 157, 231-244.	3.1	49
35	Mesoarchaean–Palaeoproterozoic stratigraphic record of the Singhbhum crustal province, eastern India: a synthesis. Geological Society Special Publication, 2012, 365, 31-49.	1.3	48
36	Constraining absolute deformation ages: the relationship between deformation mechanisms and isotope systematics. Journal of Structural Geology, 1999, 21, 1255-1265.	2.3	47

#	Article	IF	CITATIONS
37	Deformed monazite yields high-temperature tectonic ages. Geology, 2015, 43, 383-386.	4.4	47
38	Precambrian reidite discovered in shocked zircon from the Stac Fada impactite, Scotland. Geology, 2015, 43, 899-902.	4.4	47
39	Assessing the mechanisms of common Pb incorporation into titanite. Chemical Geology, 2018, 483, 558-566.	3.3	47
40	Unravelling complex geologic histories using U–Pb and trace element systematics of titanite. Chemical Geology, 2019, 504, 105-122.	3.3	46
41	Determination of high spatial resolution argon isotope variations in metamorphic biotites. Geochimica Et Cosmochimica Acta, 1997, 61, 3809-3833.	3.9	45
42	A microstructural and argon laserprobe study of shear zone development at the western margin of the Nanga Parbat-Haramosh Massif, western Himalaya. Contributions To Mineralogy and Petrology, 1997, 128, 16-29.	3.1	45
43	40Ar/39Ar ages in deformed potassium feldspar: evidence of microstructural control on Ar isotope systematics. Contributions To Mineralogy and Petrology, 2001, 141, 186-200.	3.1	45
44	A review of the geology and geodynamic evolution of the Palaeoproterozoic Earaheedy Basin, Western Australia. Earth-Science Reviews, 2009, 94, 39-77.	9.1	45
45	An investigation of the laser-induced zircon â€~matrix effect'. Chemical Geology, 2016, 438, 11-24.	3.3	44
46	Shocked monazite chronometry: integrating microstructural and in situ isotopic age data for determining precise impact ages. Contributions To Mineralogy and Petrology, 2017, 172, 1.	3.1	44
47	Time-resolved, defect-hosted, trace element mobility in deformed Witwatersrand pyrite. Geoscience Frontiers, 2019, 10, 55-63.	8.4	44
48	The effect of grain orientation on secondary ion mass spectrometry (SIMS) analysis of rutile. Chemical Geology, 2012, 300-301, 81-87.	3.3	43
49	A distant magmatic source for Cretaceous karst bauxites of Southern Apennines (Italy), revealed through SHRIMP zircon age dating. Terra Nova, 2012, 24, 326-332.	2.1	43
50	Cr-spinel records metasomatism not petrogenesis of mantle rocks. Nature Communications, 2019, 10, 5103.	12.8	42
51	Cubic zirconia in >2370 °C impact melt records Earth's hottest crust. Earth and Planetary Science Letters, 2017, 477, 52-58.	4.4	41
52	Structural evolution of the High Himalayan Gneiss sequence, Langtang Valley, Nepal. Geological Society Special Publication, 1993, 74, 375-389.	1.3	40
53	Relationship between microstructures and grain-scale trace element distribution in komatiite-hosted magmatic sulphide ores. Lithos, 2014, 184-187, 42-61.	1.4	39
54	Earth's oldest mantle fabrics indicate Eoarchaean subduction. Nature Communications, 2016, 7, 10665.	12.8	39

#	Article	IF	CITATIONS
55	Nanoscale distribution of Pb in monazite revealed by atom probe microscopy. Chemical Geology, 2018, 479, 251-258.	3.3	39
56	Atomic worlds: Current state and future of atom probe tomography in geoscience. Scripta Materialia, 2018, 148, 115-121.	5.2	39
57	An atmospheric source of S in Mesoarchaean structurally-controlled gold mineralisation of the Barberton Greenstone Belt. Precambrian Research, 2016, 285, 10-20.	2.7	38
58	Empirical constraints on shock features in monazite using shocked zircon inclusions. Geology, 2016, 44, 635-638.	4.4	38
59	Nanoscale resetting of the Th/Pb system in an isotopically-closed monazite grain: A combined atom probe and transmission electron microscopy study. Geoscience Frontiers, 2019, 10, 65-76.	8.4	38
60	The evolution of the footwall to the Ronda subcontinental mantle peridotites: insights from the Nieves Unit (western Betic Cordillera). Journal of the Geological Society, 2013, 170, 385-402.	2.1	37
61	Phase equilibria modelling constraints on <i>P–T</i> conditions during fluid catalysed conversion of granulite to eclogite in the Bergen Arcs, Norway. Journal of Metamorphic Geology, 2018, 36, 315-342.	3.4	37
62	Antimony in rutile as a pathfinder for orogenic gold deposits. Ore Geology Reviews, 2019, 106, 1-11.	2.7	37
63	Microstructural evolution and trace element mobility in Witwatersrand pyrite. Contributions To Mineralogy and Petrology, 2013, 166, 1269-1284.	3.1	35
64	The structure of and origin of nodular chromite from the Troodos ophiolite, Cyprus, revealed using high-resolution X-ray computed tomography and electron backscatter diffraction. Lithos, 2015, 218-219, 87-98.	1.4	35
65	The effects of deformation-induced microstructures on intragrain 40Ar/39Ar ages in potassium feldspar. Geology, 1999, 27, 363.	4.4	33
66	Inclusion-localised crystal-plasticity, dynamic porosity, and fast-diffusion pathway generation in zircon. Journal of Structural Geology, 2012, 35, 78-89.	2.3	32
67	Microstructural, trace element and geochronological characterization of TiO2 polymorphs and implications for mineral exploration. Chemical Geology, 2018, 476, 130-149.	3.3	32
68	Computer vision-based framework for extracting tectonic lineaments from optical remote sensing data. International Journal of Remote Sensing, 2020, 41, 1760-1787.	2.9	32
69	Novel Applications of FIB-SEM-Based ToF-SIMS in Atom Probe Tomography Workflows. Microscopy and Microanalysis, 2020, 26, 750-757.	0.4	32
70	Construction and systematic assessment of relative deformation histories. Journal of Structural Geology, 1999, 21, 1245-1253.	2.3	31
71	Palaeoproterozoic to Eoarchaean crustal growth in southern Siberia: a Nd-isotope synthesis. Geological Society Special Publication, 2009, 323, 127-143.	1.3	30
72	A new kind of invisible gold in pyrite hosted in deformation-related dislocations. Geology, 2021, 49, 1225-1229.	4.4	30

#	Article	IF	CITATIONS
73	Thermal history of the Sonnblick Dome, south-east Tauern Window, Austria: Implications for heterogeneous uplift within the Pennine basement. Geologische Rundschau: Zeitschrift Fur Allgemeine Geologie, 1993, 82, 667.	1.3	29
74	lsotopic constraints on the cooling history of the Nanga Parbat-Haramosh Massif and Kohistan arc, western Himalaya. Tectonics, 1995, 14, 237-252.	2.8	28
75	Heterogeneous excess argon and Neoproterozoic heating in the Usagaran Orogen, Tanzania, revealed by single grain 40Ar/39Ar thermochronology. Journal of African Earth Sciences, 2004, 39, 165-176.	2.0	28
76	The golden ark: arsenopyrite crystal plasticity and the retention of gold through high strain and metamorphism. Terra Nova, 2016, 28, 181-187.	2.1	28
77	Nanoscale processes of trace element mobility in metamorphosed zircon. Contributions To Mineralogy and Petrology, 2019, 174, 1.	3.1	28
78	Atom probe tomography analysis of the reference zircon gj-1: An interlaboratory study. Chemical Geology, 2018, 495, 27-35.	3.3	27
79	Bayesian geological and geophysical data fusion for the construction and uncertainty quantification of 3D geological models. Geoscience Frontiers, 2021, 12, 479-493.	8.4	27
80	Deformation-enhanced recrystallization of titanite drives decoupling between U-Pb and trace elements. Earth and Planetary Science Letters, 2021, 560, 116810.	4.4	27
81	Response of cathodoluminescence to crystal-plastic deformation in zircon. Chemical Geology, 2009, 261, 12-24.	3.3	26
82	A scanning ion imaging investigation into the micron-scale U-Pb systematics in a complex lunar zircon. Chemical Geology, 2016, 438, 112-122.	3.3	25
83	Rutile compositions in the Kalgoorlie Goldfields and their implications for exploration. Australian Journal of Earth Sciences, 2011, 58, 803-812.	1.0	22
84	Extensional episodes in the Paleoproterozoic Capricorn Orogen, Western Australia, revealed by petrogenesis and geochronology of mafic–ultramafic rocks. Precambrian Research, 2018, 306, 22-40.	2.7	22
85	Solar wind contributions to Earth's oceans. Nature Astronomy, 2021, 5, 1275-1285.	10.1	22
86	Electron backscatter diffraction analysis of zircon: A systematic assessment of match unit characteristics and pattern indexing optimization. American Mineralogist, 2008, 93, 187-197.	1.9	21
87	Evolution of zircon deformation mechanisms in a shear zone (Lanzo massif, Western-Alps). Lithos, 2011, 127, 414-426.	1.4	21
88	Mantle deformation during rifting: Constraints from quantitative microstructural analysis of olivine from the East African Rift (Marsabit, Kenya). Tectonophysics, 2013, 608, 1122-1137.	2.2	21
89	Mechanical twinning of monazite expels radiogenic lead. Geology, 2021, 49, 417-421.	4.4	21
90	Geochronology of Paleoproterozoic Augen Gneisses in the Western Gneiss Region, Norway: Evidence for Sveconorwegian Zircon Neocrystallization and Caledonian Zircon Deformation. Journal of Geology, 2013, 121, 105-128.	1.4	20

#	Article	IF	CITATIONS
91	Constraining mountain front tectonic activity in extensional setting from geomorphology and Quaternary stratigraphy: A case study from the Matese ridge, southern Apennines. Quaternary Science Reviews, 2019, 219, 47-67.	3.0	20
92	Micro- and nano-scale textural and compositional zonation in plagioclase at the Black Mountain porphyry Cu deposit: Implications for magmatic processes. American Mineralogist, 2019, 104, 391-402.	1.9	20
93	Neoproterozoic hydrothermal activity in the West Australian Craton related to Rodinia assembly or breakup?. Gondwana Research, 2019, 68, 1-12.	6.0	20
94	Volcanic SiO2-cristobalite: A natural product of chemical vapor deposition. American Mineralogist, 2020, 105, 510-524.	1.9	20
95	Mineral inclusions are not immutable: Evidence of post-entrapment thermally-induced shape change of quartz in garnet. Earth and Planetary Science Letters, 2021, 555, 116708.	4.4	20
96	Direct Observation of Nanoparticulate Goethite Recrystallization by Atom Probe Analysis of Isotopic Tracers. Environmental Science & amp; Technology, 2019, 53, 13126-13135.	10.0	19
97	Nanoscale constraints on the shock-induced transformation of zircon to reidite. Chemical Geology, 2019, 507, 85-95.	3.3	19
98	Proterozoic cooling and exhumation of the northern central Halls Creek Orogen, Western Australia: constraints from a reconnaissance 40Ar/39Ar study. Australian Journal of Earth Sciences, 2004, 51, 591-609.	1.0	18
99	Automated mapping of K-feldspar by electron backscatter diffraction and application to 40Ar/39Ar dating. Journal of Structural Geology, 2008, 30, 1229-1241.	2.3	17
100	Nanoscale deformation twinning in xenotime, a new shocked mineral, from the Santa Fe impact structure (New Mexico, USA). Geology, 2016, 44, 803-806.	4.4	16
101	Open-system behaviour of magmatic fluid phase and transport of copper in arc magmas at Krakatau and Batur volcanoes, Indonesia. Journal of Volcanology and Geothermal Research, 2016, 327, 669-686.	2.1	16
102	Zircon geochronology reveals polyphase magmatism and crustal anatexis in the Buchan Block, NE Scotland: Implications for the Grampian Orogeny. Geoscience Frontiers, 2017, 8, 1469-1478.	8.4	16
103	Analysis of Natural Rutile (TiO ₂) by Laser-assisted Atom Probe Tomography. Microscopy and Microanalysis, 2019, 25, 539-546.	0.4	16
104	The geochemical and geochronological implications of nanoscale trace-element clusters in rutile. Geology, 2020, 48, 1126-1130.	4.4	16
105	Nanoscale Isotopic Dating of Monazite. Geostandards and Geoanalytical Research, 2020, 44, 637-652.	3.1	15
106	Application of younging tables to the construction of relative deformation histories—1: Fracture systems. Journal of Structural Geology, 2000, 22, 1473-1490.	2.3	14
107	High-strain zone deformation in the southern Capricorn Orogen, Western Australia: kinematics and age constraints. Precambrian Research, 2004, 128, 295-314.	2.7	14
108	Nebula sulfidation and evidence for migration of "free-floating―refractory metal nuggets revealed by atom probe microscopy. Geology, 2017, 45, 847-850.	4.4	13

#	Article	IF	CITATIONS
109	Defining the Potential of Nanoscale Reâ€Os Isotope Systematics Using Atom Probe Microscopy. Geostandards and Geoanalytical Research, 2018, 42, 279-299.	3.1	13
110	A new method for dating impact events – Thermal dependency on nanoscale Pb mobility in monazite shock twins. Geochimica Et Cosmochimica Acta, 2021, 314, 381-396.	3.9	13
111	Neoproterozoic reworking of the Palaeoproterozoic Capricorn Orogen of Western Australia and implications for the amalgamation of Rodinia. Geological Society Special Publication, 2009, 327, 445-456.	1.3	12
112	Dislocations in minerals: Fast-diffusion pathways or trace-element traps?. Earth and Planetary Science Letters, 2022, 584, 117517.	4.4	12
113	Correlation between melting, deformation and fluid interaction in the continental crust of the High Himalayas, Langtang Valley, Nepal. Terra Nova, 1994, 6, 229-237.	2.1	11
114	Deformation in a complex crustal-scale shear zone: Errabiddy Shear Zone, Western Australia. Geological Society Special Publication, 2004, 224, 229-248.	1.3	11
115	Variation in XANES in biotite as a function of orientation, crystal composition, and metamorphic history. American Mineralogist, 2014, 99, 443-457.	1.9	11
116	The source of Dalradian detritus in the Buchan Block, NE Scotland: application of new tools to detrital datasets. Journal of the Geological Society, 2016, 173, 773-782.	2.1	11
117	Post-accretionary exhumation of the Meguma terrane relative to the Avalon terrane in the Canadian Appalachians. Tectonophysics, 2018, 747-748, 343-356.	2.2	11
118	Hall–Petch Slope in Ultrafine Grained Al-Mg Alloys. Metallurgical and Materials Transactions A: Physical Metallurgy and Materials Science, 2019, 50, 4047-4057.	2.2	11
119	Standardizing Spatial Reconstruction Parameters for the Atom Probe Analysis of Common Minerals. Microscopy and Microanalysis, 2022, 28, 1221-1230.	0.4	11
120	Constraining kinematic rotation axes in high-strain zones: a potential microstructural method?. Geological Society Special Publication, 2005, 243, 1-10.	1.3	10
121	The IGCP 509 database system: design and application of a tool to capture and illustrate litho- and chrono-stratigraphic information for Palaeoproterozoic tectonic domains, large igneous provinces and ore deposits; with examples from southern Africa. Geological Society Special Publication, 2009, 323, 27-47.	1.3	10
122	Disorientation control on trace element segregation in fluid-affected low-angle boundaries in olivine. Contributions To Mineralogy and Petrology, 2021, 176, 1.	3.1	10
123	Xenotime at the Nanoscale: Uâ€Pb Geochronology and Optimisation of Analyses by Atom Probe Tomography. Geostandards and Geoanalytical Research, 2021, 45, 443-456.	3.1	10
124	Quantitative microstructural characterization of natrojarosite scale formed during high-pressure acid leaching of lateritic nickel ore. American Mineralogist, 2009, 94, 1111-1119.	1.9	9
125	Grampian migmatites in the Buchan Block, NE Scotland. Journal of Metamorphic Geology, 2015, 33, 695-709.	3.4	9
126	Lunar samples record an impact 4.2 billion years ago that may have formed the Serenitatis Basin. Communications Earth & Environment, 2021, 2, .	6.8	9

#	Article	IF	CITATIONS
127	The initiation and development of metamorphic foliation in the Otago Schist, Part 2: evidence from quartz grain-shape data. Journal of Metamorphic Geology, 2005, 23, 443-459.	3.4	8
128	Cretaceous age, composition, and microstructure of pseudotachylyte in the Otago Schist, New Zealand Journal of Geology, and Geophysics, 2010, 53, 15-29.	1.8	8
129	Redistribution of Iron and Titanium in Highâ€Pressure Ultramafic Rocks. Geochemistry, Geophysics, Geosystems, 2017, 18, 3869-3890.	2.5	8
130	Subsurface deposition of Cu-rich massive sulphide underneath a Palaeoproterozoic seafloor hydrothermal system—the Red Bore prospect, Western Australia. Mineralium Deposita, 2018, 53, 1061-1078.	4.1	8
131	Microstructural constraints on magma emplacement and sulfide transport mechanisms. Lithosphere, 2019, 11, 73-90.	1.4	8
132	Pre-nucleation geochemical heterogeneity within glassy anatectic inclusions and the role of water in glass preservation. Contributions To Mineralogy and Petrology, 2021, 176, 1.	3.1	8
133	Atom probe microscopy of zinc isotopic enrichment in ZnO nanorods. AIP Advances, 2017, 7, .	1.3	7
134	Crystallography of refractory metal nuggets in carbonaceous chondrites: A transmission Kikuchi diffraction approach. Geochimica Et Cosmochimica Acta, 2017, 216, 42-60.	3.9	7
135	Trace-element segregation to dislocation loops in experimentally heated zircon. American Mineralogist, 2021, 106, 1971-1979.	1.9	7
136	Superimposed microstructures of pyrite in auriferous quartz veins as fingerprints of episodic fluid infiltration in the Wulong Lode gold deposit, NE China. Mineralium Deposita, 2022, 57, 685-700.	4.1	7
137	Partial retention of radiogenic Pb in galena nanocrystals explains discordance in monazite from Napier Complex (Antarctica). Earth and Planetary Science Letters, 2022, 588, 117567.	4.4	7
138	Spatial Reconstruction of Atom Probe Data from Zircon. Microscopy and Microanalysis, 2019, 25, 2536-2537.	0.4	6
139	Footprint of a large intracontinental rifting event: Coupled detrital zircon geochronology and geochemistry from the Mesoproterozoic Collier Basin, Western Australia. Precambrian Research, 2018, 318, 156-169.	2.7	5
140	Etching of fission tracks in monazite: An experimental study. Terra Nova, 2019, 31, 179-188.	2.1	5
141	Tracing Highly Siderophile Elements through Subduction: Insights from High-pressure Serpentinites and †Hybrid' Rocks from Alpine Corsica. Journal of Petrology, 2020, 61, .	2.8	5
142	Developing Atom Probe Tomography of Phyllosilicates in Preparation for Extraâ€Terrestrial Sample Return. Geostandards and Geoanalytical Research, 2021, 45, 427-441.	3.1	5
143	Electron backscatter diffraction analysis and orientation mapping of monazite. Mineralogical Magazine, 2010, 74, 493-506.	1.4	4
144	Magnetite-rutile symplectite in ilmenite records magma hydration in layered intrusions. American Mineralogist, 2022, 107, 395-404.	1.9	4

#	Article	IF	CITATIONS
145	Correlative Analysis using FIB-ToF-SIMS and Atom Probe Tomography on Geological Materials. Microscopy and Microanalysis, 2016, 22, 684-685.	0.4	2
146	Deformed monazite yields high-temperature tectonic ages: REPLY. Geology, 2016, 44, e378-e378.	4.4	2
147	Weakening the lower crust: conditions, reactions and deformation. Lithos, 2022, 422-423, 106738.	1.4	2
148	Isotopic constraints on fluid evolution and ore precipitation in a sediment-hosted Pb-Ag-Ba-Zn-Cu-Au deposit in the Capricorn Orogen, Western Australia. Applied Geochemistry, 2018, 96, 217-232.	3.0	1
149	Extreme plastic deformation and subsequent Pb loss in shocked xenotime from the Vredefort Dome, South Africa. , 2021, , .		1